Experimental and Theoretical Study of Oxygen Precipitation and the Resulting Limitation of Silicon Solar Cell Wafers

Jonas Schön, Tim Niewelt, Di Mu, Stephan Maus, Andreas Wolf, John D. Murphy, and Martin C. Schubert

***Abstract*—Commercial silicon is prone to form silicon oxide precipitates during high-temperature treatments typical for solar cell production. Oxide precipitates can cause severe efficiency degradation in solar cells. We have developed a model describing the nucleation and growth of oxide precipitates that considers silicon self-interstitial defects and surface effects influencing the precipitate growth in ∼150 μm thick wafers during the solar cell processing. This kinetic model is calibrated with experiments that cause a well-defined and strong precipitate growth to give a prediction of the carrier lifetime limitation because of the oxide precipitates. We test the oxide precipitate model with scanning Fourier-transform infrared spectroscopy, selective etching, and lifetime measurements on typical Cz solar cell wafers before and after solar cell processes. Despite the relatively rough saw damaged etched surfaces and the thin wafers, we observe recurring ring patterns in the measurements of interstitial oxygen reductions, oxide precipitate etch pit density, and recombination activity by photoluminescence imaging. The concentration of precipitated oxygen correlates with the recombination activity and with the initial interstitial oxygen concentration. However, we found lifetime measurements to be a more sensitive technique to study oxide precipitates and using these we find smaller precipitates not detected by selective etching are very recombination active too. The measured concentrations of precipitated oxygen and lifetime agree fairly well with the predictions of the model.**

***Index Terms*—Charge carrier lifetime, oxygen, photovoltaic cells, silicon.**

Manuscript received August 25, 2020; revised November 2, 2020 and December 9, 2020; accepted December 9, 2020. This work was supported in part by the German Federal Ministry for Economic Affairs and Energy BMWi within the research projects "GENESIS" under Contract 0324274C and Contract 0324274E, and in part by "POLDI" under Contract 0324079D. The work at the University of Warwick was supported by EPSRC under Grant EP/M024911/1 and Grant EP/S000763/1. *(Corresponding author: Jonas Schön.)*

Jonas Schön and Tim Niewelt are with the Fraunhofer Institute for Solar Energy Systems ISE, 79110 Freiburg im Breisgau, Germany, and also with the Laboratory for Photovoltaic Energy Conversion, Department of Sustainable Systems Engineering, University of Freiburg, 79085 Freiburg im Breisgau, Germany (e-mail: jonas.schoen@ise.fraunhofer.de; tim.niewelt@ise.fraunhofer.de).

Di Mu, Stephan Maus, Andreas Wolf, and Martin C. Schubert are with the Fraunhofer Institute for Solar Energy Systems ISE, 79110 Freiburg im Breisgau, Germany (e-mail: di.mu@ise.fraunhofer.de; stephan.maus@ise.fraunhofer.de; andreas.wolf@ise.fraunhofer.de; martin.schubert@ise.fraunhofer.de).

John D. Murphy is with the School of Engineering, University of Warwick, CV4 7AL Coventry, U.K. (e-mail: john.d.murphy@warwick.ac.uk).

Color versions of one or more of the figures in this article are available online at https://doi.org/10.1109/JPHOTOV.2020.3044353.

Digital Object Identifier 10.1109/JPHOTOV.2020.3044353

I. Introduction

OXIDE precipitates (OPs) are common defects in the Czochralski (Cz) silicon and can cause severe efficiency degradation in solar cells produced from crystal regions with a high oxygen concentration [1]–[3]. During the solar cell production, oxygen precipitation is facilitated by the combination of the cooldown after crystallization during which nuclei form, the dopant source deposition at around 800 °C ($POCl_3$) or 900–950 °C (BBr_3), which leads to precipitate sizes sufficiently large to survive a following high-temperature step at which the precipitates grow sufficient enough to limit the charge carrier lifetime. Solar cell processes without a higher temperature drive-in step after the doping deposition are usually less prone to a limitation by large oxygen precipitates.

The nucleation and growth of OP were studied in detail for the integrated circuit (IC) industry on thick wafers and under annealing conditions that are not typical for solar cells, e.g., [4]–[7]. The experimental studies are supported by computational modeling to enhance oxygen precipitation intentionally. Numerous models for oxygen precipitation have been proposed based on, for example, the Fokker–Planck equation [8] or a two-moment approach (e.g., [6]). It is known that oxygen precipitation is extremely sensitive to the initial concentrations of vacancies and self interstitials. Although the dependency of the OP kinetics on these intrinsic point defects is included in advanced models (e.g., [6], [8], [9]), the exchange of vacancies and interstitials with the wafer surfaces is often not explicitly simulated.

The numerous experimental and theoretical studies can serve as a very good basis for the optimization of solar cell process sequences by minimizing the recombination activity of OPs. However, the findings on thick wafers from the IC industry cannot be directly transferred to thin solar wafers for the following four reasons.

1) The annealing times and gas atmosphere for typical solar cell processes differ significantly from most existing experiments.
2) Cz for photovoltaic use is usually crystallized with fast pulling rates of >1.7 mm/min because of cost constraints [10]. This results in higher vacancy concentrations and possibly also affects other defects.
3) During high-temperature processes on thin wafers, the surface and the gas atmosphere become more important, e.g., because of the in-diffusion of silicon interstitials from the

surface. These effects cause a stronger depth dependence of the concentration of interstitial oxygen [O_i].

4) The aim in the IC industry was to use the OPs for gettering harmful metallic impurities away from the near-surface device region; therefore, in this context, metal-decorated OPs were desirable but the resulting enhanced recombination activity is highly undesirable for solar cells, whose active device region is often the whole wafer.

In order to assess the PV relevance of these effects, specific experiments with solar Cz wafers and typical solar cell processes are necessary. For this purpose, we have modified the scanning Fourier-transform infrared absorption (FTIR) and etch pit density (EPD) counting procedure after selective etching for thin and nonpolished wafers. This, combined with high surface passivation quality by AlO_x (and thus a reliable bulk lifetime measurement), allows a spatially resolved correlation of recombination activity with the precipitated oxygen, similar to Basnet *et a*l. [11] and [12], and OP density (EPD) on these wafers.

Furthermore, in contrast with former theoretical studies [4]–[7], the 1-D model for oxygen precipitation elaborated in this work accounts for the depth dependence and stronger influence of the surface in thinner wafers. In a first step, the model is calibrated with results of thick wafers intended for the IC devices processed in long high-temperature processes. In the next step, we compare spatially resolved measurements on solar cell wafers after a moderate thermal budget processing with the simulations. Finally, we extend our model to predict the charge carrier lifetime limitation introduced by OP after a given thermal process from the initial [O_i]. The results are compared with lifetime measurements on solar Cz wafers after a range of thermal processes.

II. Model and Calibration

A. Model

A 1-D model of the nucleation and growth of OP is elaborated in the software Sentaurus Process that already includes models for the surface oxidation and the transport and reactions of vacancies, self-interstitials (Int), and dopants. For the formation of self-interstitial clusters and stacking faults, we use the "full" Sentaurus Process model [13] with standard parameters for silicon interstitial solubility $\mathrm{Sol_{Int}}$. Given the relatively high recombination rates of interstitials and vacancies, we choose to adjust only the initial net vacancy concentration to fit the experimental results. In the OP model, the density of small OPs of size $n(f_n)$ is simulated explicitly with one differential equation per size

$$\frac{\partial f_n}{\partial t} = R_n - R_{n+1} \tag{1}$$

$$R_n = \frac{4\pi r_{n-1}^2 D_0}{a + r_{n-1}} \left([\mathrm{O_i}] f_{n-1} - \mathrm{Sol_{Oi}} \left(\frac{[\mathrm{Int}]}{\mathrm{Sol_{Int}}} \right)^{\Delta n_{\mathrm{Int}}} e^{\frac{-E_a}{k_B T \sqrt{n}}} f_n \right). \tag{2}$$

TABLE I
Model Parameters

Parameter	Quantity	Origin
E_a	8.3×10^{-4} eV/K × T	Fit
P	1.5×10^{15}	Fit
Solubility Sol_{Oi}	9×10^{22} cm^{-3} ×exp(-1.52eV/(k_BT))	[17]
O_i diffusivity D_0	0.13 cm^2/s ×exp(-2.53eV/(k_BT))	[17]
a	5Å	[6]
V_{SiO_2}	4.35×10^{-23} cm^3	[6]
V_{Si}	2×10^{-23} cm^3	[6]
μ_{Si}	64.9 GPa	[6]
K_{SiO_2}	36.9 GPa	[6]
E_t(D1)	E_V+0.22eV	[18]
E_t(D2)	E_C-0.14 eV	Fit
$\sigma_{n,D1}^{surf}$	2.3×10^{-16} cm^2	Derived from [5]
$\sigma_{p,D1}^{surf}$	1.8×10^{-18} cm^2	Derived from [5]
$\sigma_{n,D2}^{surf}$	1.2×10^{-18} cm^2	Derived from [5]
$\sigma_{p,D2}^{surf}$	1.8×10^{-15} cm^2	Derived from [5]

The used parameters for the oxygen diffusivity D_0, oxygen solubility $\mathrm{Sol_{Oi}}$, the interface reaction constant a, and the fitting parameter E_a are listed in Table I. Spherical OPs are assumed to calculate the radius r_n. The injected concentration of interstitial silicon $\Delta n_{\mathrm{Int}} = n_{\mathrm{Int_{opt}}} - (n-1)_{\mathrm{Int_{opt}}}$ during oxygen precipitation is calculated as suggested by Trzynadlowski and Dunham [6]

$$n_{\mathrm{Int_{opt}}} = \frac{n}{2} \left[\frac{3}{4} k_B T \times \ln \left(\frac{\mathrm{Sol_{Int}}}{[\mathrm{Int}]} \right) \times \left(\frac{V_{\mathrm{SiO_2}}}{V_{\mathrm{Si}}^2 \mu_{\mathrm{Si}}} \right) \times \left(1 + \frac{4\mu_{\mathrm{Si}}}{3K_{\mathrm{SiO_2}}} \right) + \frac{V_{\mathrm{SiO_2}}}{V_{\mathrm{Si}}} - 1 \right] \tag{3}$$

with the silicon atomic volume V_{Si}, the silicon shear modulus μ_{Si} , the molecular volume V_{SiO2}, and the bulk modulus K_{SiO2} listed in Table I. In our model, the effective O_i solubility in the vicinity of OPs depends on the square root of the number of oxygen atoms in the precipitate to account for the higher chemical potential of oxygen atoms in a small precipitate than in a large precipitate. This approach was already successfully applied for the simulation of Fe precipitates [14]. Precipitates with $m = 72$ or more oxygen atoms are simulated with the two-moment approach, i.e., by solving differential equations for the density of larger precipitates f_D and the overall oxygen concentration in larger precipitates f_C

$$\frac{\partial f_D}{\partial t} = R_m \tag{4}$$

$$\frac{\partial f_C}{\partial t} = m \times R_m + R_{n_{\mathrm{avg}}} \tag{5}$$

$$R_{n_{\mathrm{avg}}} = \frac{4\pi r_{n_{\mathrm{avg}}-1}^2 D_0}{a + r_{n_{\mathrm{avg}}-1}} \times \left([\mathrm{O_i}] - \mathrm{Sol_{Oi}} \left(\frac{[\mathrm{Int}]}{\mathrm{Sol_{Int}}} \right)^{\Delta n_{\mathrm{avg_{Int}}}} e^{\frac{-E_a}{k_B T \sqrt{n_{\mathrm{avg}}}}} \right) \times f_D \tag{6}$$

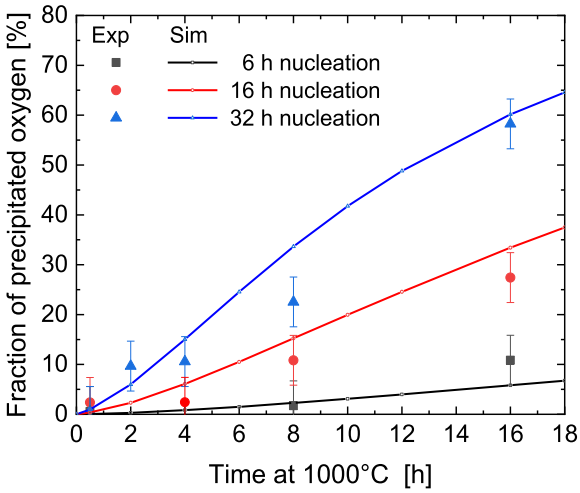

Fig. 1. Measured (points) and simulated (curves) concentration of precipitated oxygen divided by the total oxygen concentration of 7.7×10^{17} cm^{-3}.

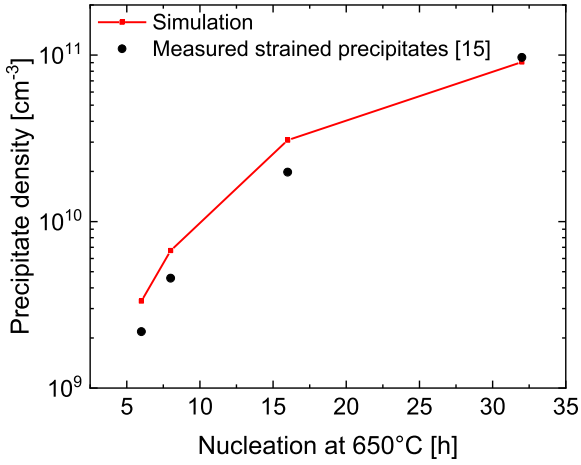

Fig. 2. Measured and simulated density of the OP density for an initial oxygen concentration of 7.7×10^{17} cm^{-3}. Measured data are taken from [15].

with n_{avg} describing the average number of oxygen atoms in a precipitate and $\Delta n_{\mathrm{avgInt}}$ the average injected interstitial Si atoms.

For the smallest precipitates f_1, we use the following boundary condition:

$$R_1 = \frac{4\pi r_1^2 D_0}{a + r_1} \times \left([\mathrm{O_i}] \times P - \mathrm{Sol_{Oi}} \left(\frac{[\mathrm{Int}]}{\mathrm{Sol_{Int}}} \right)^{0.5} e^{\frac{-E_a}{k_B T}} \times f_1 \right) \tag{7}$$

with the fitting parameter P necessary for the deviation from homogeneous nucleation [7] (see Table I).

B. Calibration Using Integrated Circuit Material

To enable a predictive model, which is as general as possible, we calibrate our model with the help of experiments with well-defined starting conditions and long intentional OP growth resulting in well-defined quantitative measurement results. We fit the free parameters of the model E_a and P to the measurements performed on 700 μm thick samples with an initial interstitial oxygen concentration of $7.7 \pm 0.2 \times 10^{17}$ cm^{-3} originating from the experiment series underlying [4] and [15]. As described in detail in [15], the wafers were subjected to a homogenization anneal to dissolve all grown-in precipitates followed by a nucleation step at 650 °C for 6–32 h to create OP nuclei with different densities. A subsequent 4 h anneal at 800 °C shifts the precipitate size to sizes sufficiently large to survive the following 1000 °C growth anneal. The simulation results are almost invariant for the initial net vacancy concentrations between 0 and 1×10^{11} cm^{-3} and we choose an initial net vacancy concentration of 1×10^{10} cm^{-3} in the results presented. With the model parameters P and E_a from Table I, a satisfactory agreement between measured and simulated data is achieved. An example is shown in Fig. 1 for the fraction of precipitated oxygen derived from FTIR measurements in dependence of the nucleation and the growth time. Longer high-temperature annealing results in a larger OP, whereas longer nucleation time leads to a higher OP density. After 32 h of nucleation and 16 h of at 1000 °C, 60% of the oxygen is precipitated in measurements and the simulation.

OPs undergo a morphological transformation as they grow from an unstrained to a strained state [4], [16]. Strained OPs can be revealed by preferential etching and the resulting EPD can be estimated from optical microscopy. The EPD was measured after the longest high-temperature precipitate growth anneal (16 h at 1000 °C), at which almost all precipitates were strained [15]. In Fig. 2, we compare the OP density in [13] after these with the simulated OP density of this work. We use the simulated densities of all OPs that have 72 or more oxygen atoms. However, this cutoff has almost no influence on the results shown in Fig. 2, where all OPs are very large. As expected, the precipitate density depends strongly on the nucleation time, i.e., the time at 650 °C. The simulated OP density is in very good agreement with the measurement data from [13]. In principle, a slightly higher simulated precipitate density for shorter nucleation times could be explained by a relatively higher concentration of unstrained precipitates, which are not revealed by chemical etching and hence do not contribute to the measured EPD.

III. Experiments

In order to test the 1-D model, we characterize thin wafers from our experiments on the impact of diffusion processes [19].

A. Samples and Processing

We investigate four sets of industrial PV n- and p-type Cz wafers with different oxygen concentrations. To ensure a very low oxygen concentration, one of the sample sets was grown by the magnetic Cz process (designated as mCz-Si). The sets each consist of several sister wafers treated in nine different thermal process sequences of varied duration, peak temperature, and ambient atmosphere (see Table III and [19] for process details). Table II summarizes the interstitial oxygen concentration and resistivity of the wafer sets as measured on a sample after a thermal process to dissolve thermal donors. This was realized

TABLE II
MATERIAL OVERVIEW

Material	ρ	$O_{i,initial}$	Sample thickness
p-type Cz-Si	2.0 Ωcm	9.5×10^{17} cm^{-3}	132±5 µm
p-type mCz-Si	0.6 Ωcm	2.8×10^{17} cm^{-3}	152±5 µm
n-type Cz-Si	10.5 Ωcm	11×10^{17} cm^{-3}	170±5 µm
n-type Cz-Si	5.9 Ωcm	4.3×10^{17} cm^{-3}	151±5 µm

TABLE III
PROCESS OVERVIEW

Process	$POCl_3$	Drive-in	Drive-in gas
only POCl	800°C	-	-
O_2 860°C 12 min	800°C	12 min 860°C	O_2
N_2 860°C 12 min	800°C	12 min 860°C	N_2
O_2 860°C 120 min	800°C	120 min 860°C	O_2
N_2 860°C 120 min	800°C	120 min 860°C	N_2
O_2 1050°C 12 min	800°C	12 min 1050°C	O_2
N_2 1050°C 12 min	800°C	12 min 1050°C	N_2
O_2 1050°C 120 min	800°C	120 min 1050°C	O_2
N_2 1050°C 120 min	800°C	120 min 1050°C	N_2

by a typical $POCl_3$ deposition process at ∼800 °C in a tube furnace. Similar resistivities were measured after processes with an additional 860 or 1050 °C step. After the $POCl_3$ process, the wafers have high charge carrier lifetimes (see Fig. 9) and no ring structure in photoluminescence (PL). The impact of high-temperature solar cell processes, e.g., an emitter drive-in, is investigated by the combination of the aforementioned step ("$POCl_3$ deposition") directly followed by 12 or 120 min at 860 or 1050 °C. The thermal processes were tested featuring two different gas atmospheres during the drive-in step, namely, O_2 and N_2. A surface oxidation is known to force further interstitial silicon atoms to diffuse from the SiO_2/silicon interface into the wafer bulk, which might influence the precipitation. After all processes, the resulting phosphosilicate glass (PSG) layer and diffused regions were etched off and the wafers passivated via the atomic layer deposition of Al_2O_3 on both sides followed by a 10 min annealing at 400 °C in forming gas. This treatment is known to provide good surface passivation with surface recombination velocities below 4 cm/s. The resulting wafer thicknesses range between 130 and 170 μm.

The injection-dependent charge carrier lifetime was measured with a quasi-steady-state photo conductance (QSSPC). Between the passivation activation anneal and the measurements, the samples were stored in the dark to keep boron oxygen defects in p-type samples in the deactivated state [20]. In addition, photoluminescence imaging at a constant illumination was performed and on the selected samples calibrated to lifetime image stacks via modulated photoluminescence measurements [21]. For these selected samples, the lifetime images at a fixed injection (5×10^{13} cm^{-3}) were interpolated for wafers with ($\tau_{\mathrm{POCl+drive\text{-}in}}$) and without ($\tau_{\mathrm{POCl}}$) drive-in process. The difference in the lifetime at a fixed injection between these samples can be assessed in terms of a normalized defect density $N_t* = 1/\tau_{\mathrm{POCl+drive\text{-}in}}$ - $1/\tau_{\mathrm{POCl}}$ [22] created during the drive-in step. After the 12 min oxidation at 1050 °C an average interstitial iron concentration of 2×10^{10} cm^{-3} was measured with the Fe_i imaging [23] in p-type Cz-Si, which is rather low compared with Murphy *et al*. [24].

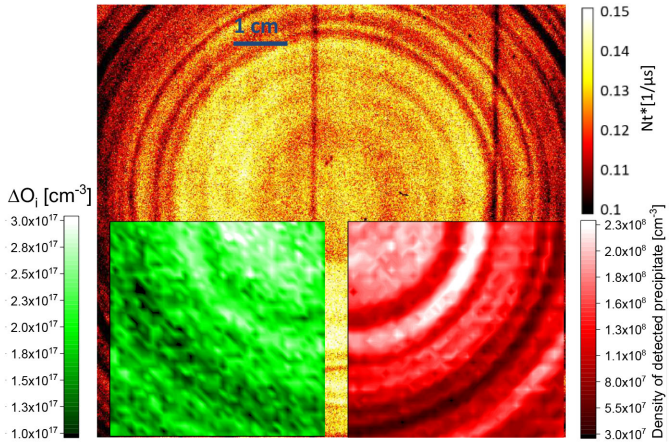

Fig. 3. Precipitate density measured by EPD (red scale bottom right) and change of interstitial oxygen concentration (green scale bottom left) during 120 min oxidation at 1050 °C in the n-type wafer with $[O_{i,initial}] = 1.1\times10^{18}$ cm^{-3}. The effective defect density $N_t{}^*$ (background, hot scale, top) was measured for a sister wafer at a constant injection density of 5×10^{13} cm^{-3}.

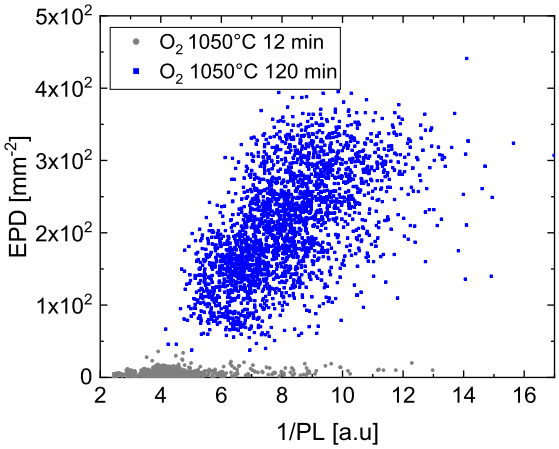

Fig. 4. Correlation of precipitate density calculated from EPD and inverse PL signal (1/PL) after 12 and 120 min oxidation at 1050 °C in two n-type samples.

B. Precipitate Density

A set of samples were subjected to an etching step in a Secco etch (50% HF and potassium dichromate solution) that confers preferential etching for the strained silicon in the vicinity of the OPs. Because of the rough surface structure after the damage etch, special care has been taken to avoid the false detection of spurious local surface structures. From the EPD we assess the precipitate density distribution, as shown in the red scale inset of Fig. 3 (bottom right). We observe an overall good match with the distribution of $N_t{}^*$ found on sister wafers (background image in the hot scale), which demonstrates the applicability of the method on wafers with a rough surface structure, i.e., without mechanical polishing.

For a further analysis of the sensitivity of the methods, we locally correlate the inverse PL difference ($1/\Delta\mathrm{PL} = 1/\mathrm{PL}_{\mathrm{POCl+drive\text{-}in}}$ - $1/\mathrm{PL}_{\mathrm{POCl}}$) as a qualitative measure of N_t* with the measured OP density (EPD) on the same wafers (see Fig. 4). We found that the PL counts without drive-in are more

than two orders of magnitude higher compared with the PL counts after drive-in and, thus, neglectable compared with other uncertainties of the measurement. Thus, $1/\mathrm{PL}_{\mathrm{Process}}$ is plotted instead of $1/\Delta\mathrm{PL}$ in Fig. 4. A clear increase of the precipitate density is observed with increasing defect concentration after 120 min oxidation at 1050 °C (blue dots). For a test of our measurement procedure on wafers after industrial-type solar cell processes, we investigate a wafer after only 12 min oxidation at 1050 °C (gray squares). The PL image of this wafer shows strong ring patterns but we expect much smaller precipitate sizes because of the shorter drive-in process. According to our simulations, the average precipitate radius is only ∼15 nm compared with ∼25 nm after 120 min oxidation. The correlation for both wafers in Fig. 4 indicates that zero EPD detected precipitate density does not ensure an unchanged PL intensity, which would correspond to the negligible values of the 1/PL signal in Fig. 4. This indicates a significant recombination activity by the precipitates that were not detected with EPD. It should be noted that former EPD studies with mechanically polished samples might have a higher sensitivity compared with our measurements on samples with remaining saw damage grooves, where tiny etch pits might have too small contrast for automated counting. The methods featuring a higher spatial resolution, such as micro-Raman, might be capable of detecting an additional share of small precipitates [12] and, thus, could help to understand the evolution of small precipitates.

C. Change of the Oxygen Concentration $\Delta[O_i]$

After the $POCl_3$ deposition, most dissolved oxygen is expected to be in an interstitial state, where it is not recombination active. The interstitial oxygen concentration was measured via scanning FTIR at 41 × 41 spots in a 4 × 4 cm^2 area with one corner in the wafer center. FTIR is known to be a reliable method to investigate the interstitial oxygen concentration in mechanically polished thick silicon but is challenging for the investigation of substrates as thin as the samples investigated in this work. The spectra were analyzed with an evaluation procedure derived from the DIN 50438-1B norm. We found that lateral scans on our samples were mostly affected by thickness variations, such as saw damage grooves. To account for the sample thickness variations, we determined local sample thickness d from the absorption at 614 cm^{-1} (A_{614}) caused by the Si–Si phonon absorption.

The green scale inset of Fig. 3 (bottom left) demonstrates the applicability of the scanning FTIR method to determine the spatially resolved concentration of precipitated oxygen in the thin and rough wafers used for PV cells. It depicts the local difference $\Delta[\mathrm{O_i}]$ between a sample after drive-in and the sister sample before drive-in. The precipitated oxygen exhibits a ring pattern similar to the ones in the effective defect density and the OP density images. An advantage of the spatially resolved measurements of $\Delta[\mathrm{O_i}]$ is the extraction of trends within a single wafer. The pointwise comparison for the wafer after 120 min oxidation at 1050 °C exhibits a clear correlation between $\Delta\mathrm{O_i}$ and the inversed PL signal, as shown in Fig. 5 (Pearson correlation coefficient of 0.96). An exact linear behavior is not

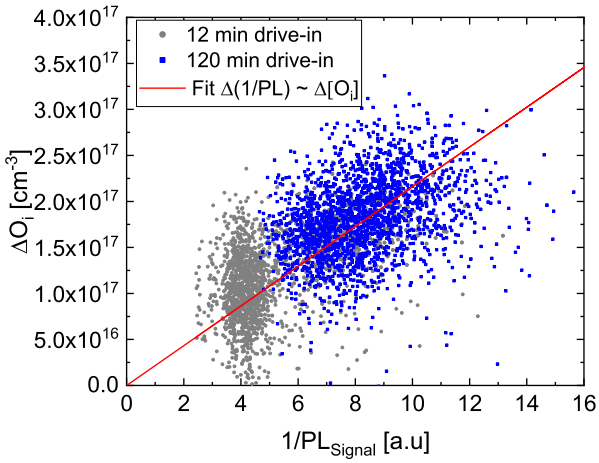

Fig. 5. Correlation of precipitated oxygen ($\Delta\mathrm{O_i}$) and inverse PL signal (1/PL) in two n-type samples with an initial $[\mathrm{O_i}]$ of 1.1×10^{18} cm^{-3}.

expected because of the nonlinearity between PL and lifetime. Together with the scatter this does not allow to distinguish between a linear correlation and the correlation to $(\Delta[\mathrm{O_i}])^{2/3}$ predicted from [5] for a constant precipitate density, i.e., no further nucleation at 1050 °C.

Within the wafer, after 12 min oxidation at 1050 °C, no clear trend is found likely because of the strong noise. However, the trend of the 120 min wafer continues. One reason for the scatter is the inhomogeneous distribution of OP and the resulting smearing in the PL images because of the carrier diffusion toward regions containing more recombination active OP.

IV. Simulation of Solar Cell Processes

In this section, we compare the measurements on thin "solar" wafers from Section III with our simulations. The initial condition of defect precursors and intrinsic defects is not well-defined for such wafers. Therefore, we start our simulations with the cooldown after crystallization to reduce this uncertainty and to analyze the influence of the cooldown ramp. We assume a cooling rate of 2 K/min for temperatures below 900 °C, which is in the range of typical cooling rates for a solar grade Cz silicon [25]. The influence of the cooling rate on the simulated precipitate density is shown in the supplementary material. The solar grade Cz is usually pulled with high pulling rates because of the maximized throughput, which leads to high vacancy concentrations [26]. This vacancy surplus is considered with an adapted initial net vacancy concentration of 2×10^{12} cm^{-3} in the simulations.

For all simulated processes, we observe a strong impact of the interaction of intrinsic point defects with the wafer surface. Vacancies are consumed by the growing OP and diffuse from the silicon surface into the bulk, whereas interstitials are too slow for out-diffusion and form clusters and other extended crystal defects. The effect on the concentrations of the different species is demonstrated by the depth profiles, as shown in Fig. 6. After 12 min at 1050 °C, the concentration of precipitated oxygen is the orders of magnitude higher compared with the other

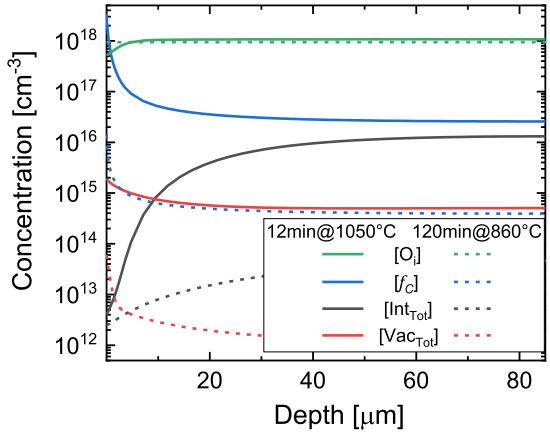

Fig. 6. Simulated depth profiles for O_i, oxygen concentration in larger precipitates f_C, total (dissolved + clustered) interstitial concentration, and vacancy concentration. The profiles are shown exemplarily for the simulated 12 min oxidation at 1050 °C with an initial $[O_i]$ of 1.1×10^{18} cm^{-3} and the simulated 120 min oxidation at 860 °C with an initial $[O_i]$ of 9.4×10^{17} cm^{-3} from the wafer surface to the center of the 170 μm thick wafer.

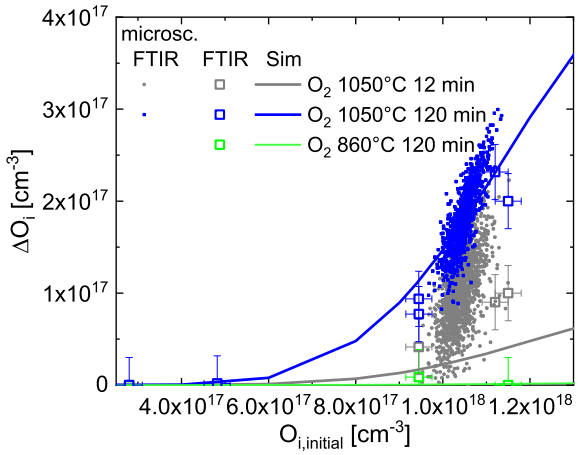

Fig. 7. Comparison of measured and simulated interstitial oxygen loss versus the oxygen concentration before drive-in $O_{i,initial}$.

process at 860 °C and, thus, much larger interstitial clusters are generated. As a consequence of the interstitial enrichment, the concentration of precipitated oxygen decreases toward the center of the wafer. A higher interstitial concentration suppresses the precipitate growth that produces interstitials and consumes vacancies. Even the $[O_i]$ is influenced and decreases toward the surface for the processes with a significant fraction of precipitated oxygen. Our model takes the influences of the depth profiles of self defects on the resulting precipitate growth into account.

Note that within the first 1–2 μm, i.e., the region dominated by direct oxygen diffusion toward the silicon surface, the simulated concentration of precipitated oxygen is probably not correct because of the complexities associated with oxygen incorporation into the surface oxide. However, a few micrometers were always etched off in the experiments before the measurements. Therefore, these regions were also discarded in the depth-averaged simulation results presented in the following section.

A. ΔO_i Comparison

In Fig. 7, the simulated $\Delta[O_i]$ for the different samples after oxidation for 12 min at 1050 °C, 120 min at 1050 °C, or 120 min at 860 °C is compared with FTIR measurements in the center area of the wafers. The measured $\Delta[O_i]$ after 120 min at 860 °C drive-in did not exceed our detection limit in accordance with the simulations. The simulations appear to underestimate the $\Delta[O_i]$ for 12 min oxidation at 1050 °C, whereas the simulations and measurements fit well after the 120 min oxidation at 1050 °C. In addition to the averaged FTIR measurements (depicted as squares with uncertainty bars), the graph also includes spatially resolved FTIR measurements (as small points) from two samples oxidized for 12 or 120 min at 1050 °C. The two data clouds are clearly separated for the different oxidation times indicating pronounced precipitation with prolonged oxidation. The local $\Delta[O_i]$ is smaller in regions with a low initial $[O_i]$. This trend appears to be even steeper in the spatially resolved measurements on single wafers compared with averaged measurements and simulations.

B. Lifetime Comparison

The charge carrier lifetime is the crucial parameter for the impact of OP on solar cell performance. Thus, our goal is a direct prediction of the lifetime from the precipitation model, which, so far, provides us with the density and average size of OP. The recombination activity of OPs in the n- and p-type silicon was studied in several publications [3], [5], [27], [28], and a reasonable empirical description was achieved assuming the superposition of two Shockley–Read–Hall (SRH) defects. A linear dependency between the defect densities N_T and the surface of large OPs was found in [5]

$$N_T \sim [\mathrm{OP}]^{1/3} \times (\Delta O_i)^{2/3} \underline{\underline{\mathrm{def}}} N_{T,\mathrm{eff}}^{\mathrm{surf}} \tag{8}$$

with the effective defect density $N_{T,\mathrm{eff}}^{\mathrm{surf}}$ relating to the precipitate surface area. The recombination activity seems to be influenced by the precipitation process [5] and impurity decoration [24], as well. The influence of the specific precipitation process can in principle be explained with recombination active OPs that are not detected by etch pit counting. This could occur if they create no or not enough strain in their vicinity to give rise to preferential etching. Thus, we choose the process with 16 h precipitate growth at 1000 °C (process *A* in [5]), where almost all precipitates are expected to grow large enough for the etch pit detection to assess the effective capture cross section of electrons and holes $\sigma_{n/p,T}^{\mathrm{surf}}$

$$N_T \times \sigma_{n/p,T} = N_{T,\mathrm{eff}}^{\mathrm{surf}} \times \sigma_{n/p,T}^{\mathrm{surf}}. \tag{9}$$

The effective capture cross sections extracted with (9) from [5] and [18] for both OP defects are listed in Table I.

We use the precipitate densities and average sizes from the simulations, as shown in Fig. 7, as the input for the prediction of the lifetime. We calculate the overall precipitate surface of all precipitate with more than $m = 72$ oxygen atoms following the cutoff from the kinetic model. However, the exact m value is not

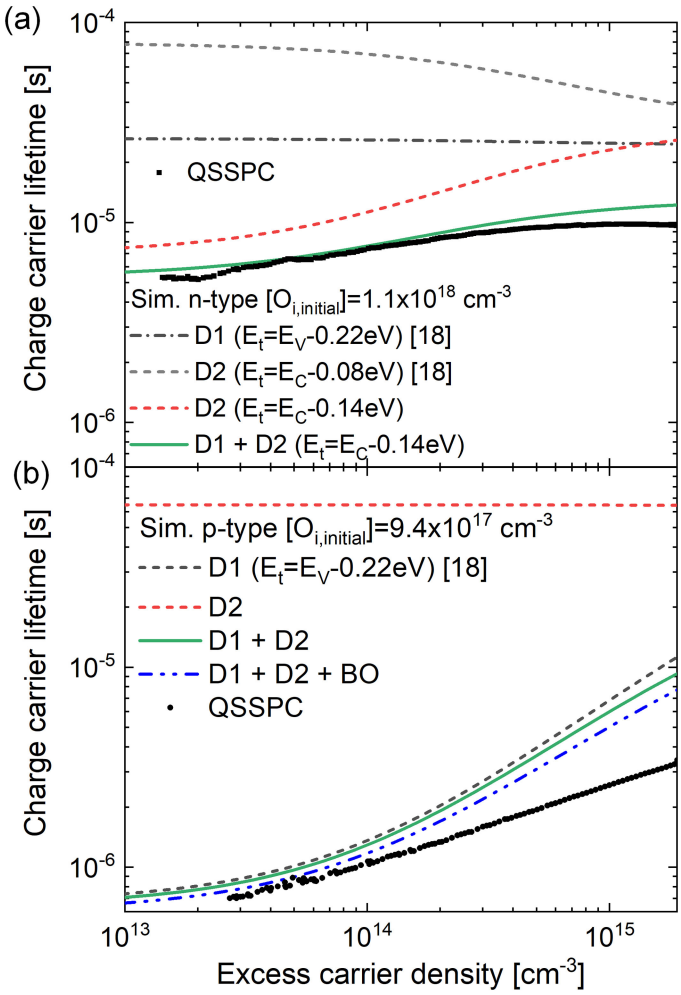

Fig. 8. QSSPC measured and simulated injection-dependent charge carrier lifetime after the $POCl_3$ diffusion and 120 min oxidation at 1050 °C. (a) n-type wafer with an initial O_i concentration of 1.1×10^{18} cm^{-3}. (b) p-type wafer with an initial O_i concentration of 9.4×10^{17} cm^{-3}. Except for the $D2$ trap level E_t, all input parameters are taken from the literature or the independent simulations shown in Fig. 7.

critical because the densities of more than 10^{11} cm^{-3} would be necessary for small precipitates to influence the charge carrier lifetime.

In Fig. 8(a), the simulated injection-dependent lifetime limitation because of OP for the n-type sample with $[O_{i,initial}] = 1.1\times10^{18}$ cm^{-3} after the 120 min oxidation process at 1050 °C is compared with lifetime measurements. With the trap levels from [18], the injection dependence of the lifetime limitation in the n-type silicon because of defect $D1$ is flat, while defect $D2$ causes a lifetime decreasing with excess carrier density. In contrast, the measured lifetimes in our n-type samples are increasing with excess carrier density. A similar injection dependence of the lifetime can be found for comparable doping levels and lifetime limitations in [27] and [28]. From this observation, we conclude that a trap level deeper in the bandgap would provide a better description of the present OP. We found that using a $D2$ trap level of 0.14 eV below the conduction band in the simulated lifetime results is a fairly good agreement with the injection dependent measurements and the overall limitation because of SiO_2. It is worth noting that the samples in [18] were passivated with SiN_x, which likely introduces more hydrogen into the wafer than the AlO_x used in this study. Thus, an explanation for the discrepancy to the levels found in [18] might be the hydrogen passivation of the deep level traps [29].

In Fig. 8(b), the simulated injection-dependent lifetime for the p-type sample after the 120 min oxidation process at 1050 °C with $[O_{i,initial}] = 9.4\times10^{17}$ cm^{-3} is compared with the lifetime measurement. Because of its capture cross sections, defect $D2$ has almost no influence on the simulated lifetime in the p-type sample independent of whether we use the original trap level from the literature or the adapted one. The parameters for $D1$ alone provide a reasonable agreement with the measured data without any adjustment. At this point, it is worth noting that the p-type silicon is more vulnerable to the effects of many contaminants (such as interstitial iron). The samples were not intentionally subjected to prolonged illumination prior to measurement to avoid the activation of boron oxygen defects. To estimate the potential influence of unintended illumination during the sample handling and characterization, the expected impact of full boron oxygen defect activation was estimated with the parameterizations from [20] and [30] and a thermal processing enhancement factor of three.

In the next step, we compare the simulated and measured lifetime at a fixed excess carrier density $\Delta n = 10^{15}$ cm^{-3} for the different samples and processes. The impact of residual bulk and surface recombination is considered in the simulations via the addition of the recombination measured on a sample after applying only the deposition process ("only POCl"). This is likely a lower estimation because the drive-in step could cause the contamination or backdiffusion of impurities from the emitter [31]. Additional impurities introduced to the wafer might also decorate the OP or form other recombination active defects.

For the p- and n-type samples, the simulations predict a small but measurable lifetime reduction after 12 min at 860 °C in the O_2 or N_2 atmosphere matched well by the measurements (see Fig. 9). After the 120 min drive-in at 860 °C, the measured lifetime drops by more than one order of magnitude to $\sim$10 μs (p-type) and $\sim$40 μs (n-type) with strong variations between sister samples and across each wafer. The simulated lifetimes after 120 min at 860 °C are a factor of ten higher compared with the measured average lifetimes. The reasons could be either a mismatch in our model for this specific temperature, i.e., a too slow OP growth during oxidation at 860 °C or process issues, e.g., contamination or unplanned process variations. To decide which explanation is more likely we repeated the process with 120 min oxidation at 860 °C in another furnace with the p-type wafers that were cut out of the crystal close to the wafers from the first experiment with $[O_{i,initial}] = 9.5\times10^{17}$ cm^{-3}. The blue symbol in Fig. 9 shows that these wafers have much higher lifetimes compared with the former experiment after the $POCl_3$ deposition at 800 °C and the following 120 min oxidation at 860 °C. This is a strong indication of process issues. At 860 °C, the oxidation process might also be very sensitive on the initial oxygen concentration and the temperature profile; slightly higher temperatures or oxygen concentration in the first process

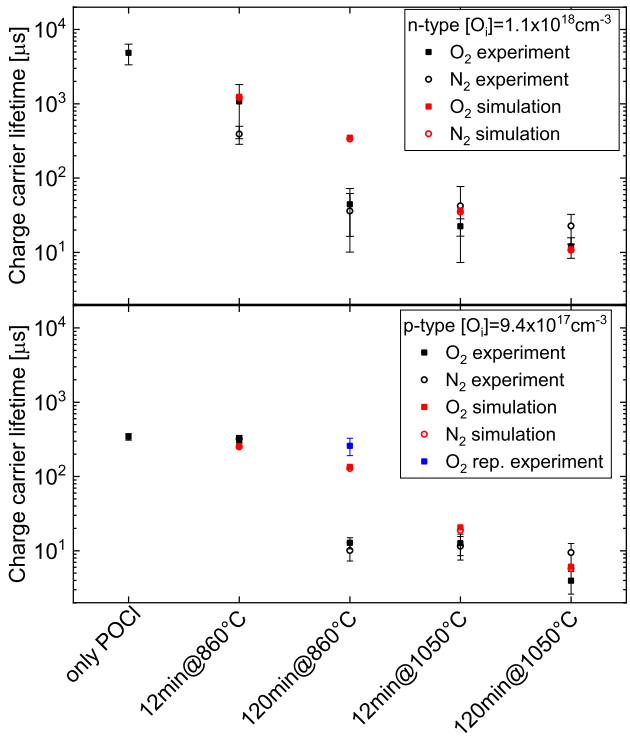

Fig. 9. Comparison of the measured and simulated lifetime at an excess carrier density of 10^{15} cm^{-3} after the $POCl_3$ deposition and a following drive-in under the listed conditions.

might explain the variation to the second experiment and the simulations.

For all drive-in processes at 1050 °C, we again see a fair agreement between simulated and measured lifetimes. The simulated lifetime is 22 μs (p-type) and 40 μs (n-type) after 12 min oxidation at 1050 °C and roughly a third of that after 120 min oxidation, respectively. The measured lifetime is two to three times smaller after 120 min compared with 12 min at 1050 °C. This reflects the differences in measured and simulated $\Delta[O_i]$ (see Fig. 7).

The simulation predicts the lifetime after processing in nitrogen to be up to 10% lower compared with the same process in oxygen atmosphere. The reason is the enhanced vacancy in-diffusion from the surface compared with the enhanced interstitial in-diffusion during oxidation. However, the simulated lifetime differences are small and within the uncertainties of the measurements and model parameters. In the experiment, the OP is already large after the $POCl_3$ (an oxidizing atmosphere) process and enough interstitial clusters are grown. As a consequence, further growth of OP and interstitial clusters at high temperature is only slightly influenced by the silicon self-defect concentrations. In contrast, experiments and simulations with the varying gas atmosphere at earlier processing steps, i.e., during the nucleation and growth of small precipitates, reveal a strong influence of the gas atmosphere on the nucleation and growth kinetics of OP (e.g., [32]).

The measured lifetime for the samples with a low initial oxygen concentration (2.8 and 4.3×10^{17} cm^{-3}) is not shown in the figure because it was found to be almost independent of the drive-in step. A drop in the lifetime was measured only after processes with a long 1050 °C drive-in. In these cases, we determine an average lifetime limitation of $\sim$700 μs (p-type) and $\sim$2 ms (n-type) because of the defects generated during 120 min drive-in at 1050 °C. However, no clear rings are visible in these samples indicating a lifetime limitation by other defects. In agreement with this observation, we simulate lifetime limitation because of OP of 3 ms or more for low oxygen samples after all drive-in processes. Because of the high lifetime and low EPD in the low oxygen samples, we can exclude a significant increase of misfit dislocations during phosphorus in-diffusion [33] as an alternative explanation of the observed lifetime degradation in samples with a high oxygen concentration.

V. Conclusion

Despite the challenges arising from the analysis of thin wafers with rough surfaces, we have found a spatially resolved correlation between precipitated oxygen concentration measured via FTIR, EPD, and $N_t{}^*$ respective 1/PL. The comparison of the measurements indicate significant recombination activity of smaller precipitates that were not detected after preferential etching because of insufficient strain in the surrounding areas. The good agreement of our numerical precipitate model with both $\Delta[O_i]$ and lifetime measurements demonstrated the successful consideration of silicon self defects and surface effects in our precipitate model. The prediction of the OP charge carrier lifetime limitation is enabled by coupling the OP model with the SRH parameters for OP from [5] modified by a slightly deeper *D*2 defect. The verified oxide growth model enabled us to analyze the OP growth in solar cell processing and overcome OP limitations by systematic mitigation strategies.

Acknowledgment

The authors would like to thank M. Müller from TUBA Freiberg and A. Haarahiltunen from Aalto University for fruitful discussions, P. Barth for chemical processing, and B. Hamman for the support during N_t measurements.

References

[1] J. Veirman *et al.*, "Thermal history index as a bulk quality indicator for Czochralski solar wafers," *Sol. Energy Mater. Sol. Cells*, vol. 158, pp. 55–59, 2016.

[2] L. Chen *et al.*, "Effect of oxygen precipitation on the performance of Czochralski silicon solar cells," *Sol. Energy Mater. Sol. Cells*, vol. 95, no. 11, pp. 3148–3151, 2011.

[3] J. Haunschild, I. E. Reis, J. Geilker, and S. Rein, "Detecting efficiency-limiting defects in Czochralski-grown silicon wafers in solar cell production using photoluminescence imaging," *Phys. Status Solidi RRL*, vol. 5, no. 5/6, pp. 199–201, 2011.

[4] R. Falster, V. V. Voronkov, V. Y. Resnik, and M. G. Milvidskii, "Thresholds for effective internal gettering in silicon wafers," in *Proc. Electrochem. Soc., High Purity Silicon 8th*, 2004, pp. 188–201.

[5] J. D. Murphy *et al.*, "The effect of oxide precipitates on minority carrier lifetime in n-type silicon," *J. Appl. Phys.*, vol. 118, no. 21, 2015, Art. no. 215706.

[6] B. C. Trzynadlowski and S. T. Dunham, "A reduced moment-based model for oxygen precipitation in silicon," *J. Appl. Phys.*, vol. 114, 2013, Art. no. 243508.

[7] H. Takeno, T. Otogawa, and Y. Kitagawara, "Practical computer simulation technique to predict oxygen precipitation behavior in Czochralski silicon wafers for various thermal processes," *J. Electrochem. Soc.*, vol. 144, no. 12, pp. 4340–4345, 1997.

[8] S. Kobayashi, "A model for oxygen precipitation in Czochralski silicon during crystal growth," *J. Cryst. Growth*, vol. 174, no. 1/4, pp. 163–169, 1997.

[9] V. V. Voronkov and R. Falster, "Grown-in microdefects, residual vacancies and oxygen precipitation bands in Czochralski silicon," *J. Cryst. Growth*, vol. 204, no. 4, pp. 462–474, 1999.

[10] S. Riepe *et al.*, "Cast-Mono silicon wafers for a sustainable PV market growth," in *Proc. 37th Eur. PV Sol. Energy Conf. Exhib.*, 2020, pp. 121–125.

[11] R. Basnet, S. P. Phang, C. Sun, F. E. Rougieux, and D. Macdonald, "Onset of ring defects in n-type Czochralski-grown silicon wafers," *J. Appl. Phys.*, vol. 127, no. 15, 2020, Art. no. 153101.

[12] R. Basnet *et al.*, "Ring defects in n-type Czochralski-grown silicon: A high spatial resolution study using Fourier-transform infrared spectroscopy, micro-photoluminescence, and micro-Raman," *J. Appl. Phys.*, vol. 124, no. 24, 2018, Art. no. 243101.

[13] Sentaurus Process L-2016.03: Synopsys, 2016.

[14] A. Haarahiltunen, H. Väinölä, O. Anttila, M. Yli-Koski, and J. Sinkkonen, "Experimental and theoretical study of heterogeneous iron precipitation in silicon," *J. Appl. Phys.*, vol. 101, no. 4, 2007, Art. no. 043507.

[15] J. D. Murphy, K. Bothe, M. Olmo, V. V. Voronkov, and R. J. Falster, "The effect of oxide precipitates on minority carrier lifetime in p-type silicon," *J. Appl. Phys.*, vol. 110, no. 5, 2011, Art. no. 053713.

[16] W. Bergholz *et al.*, "A study of oxygen precipitation in silicon using high-resolution transmission electron microscopy, small-angle neutron scattering and infrared absorption," *Philos. Mag. B*, vol. 59, no. 5, pp. 499–522, 1989.

[17] J. C. Mikkelsen, S. J. Pearton, J. W. Corbett, and S. J. Pennycook, *Oxygen, Carbon, Hydrogen, Nitrogen Crystalline Silicon*. Pittsburgh, PA, USA: Materials Research Soc., 1986.

[18] J. D. Murphy, R. E. McGuire, K. Bothe, V. V. Voronkov, and R. J. Falster, "Minority carrier lifetime in silicon photovoltaics: The effect of oxygen precipitation," *Sol. Energy Mater. Sol. Cells*, vol. 120, pp. 402–411, 2014.

[19] S. Maus *et al.*, "Impact of $POCl_3$ diffusion process parameters on oxygen precipitation in Czochralski-grown silicon," in *Proc. 36th Eur. PV Sol. Energy Conf. Exhib.*, 2019, pp. 151–156.

[20] T. Niewelt, J. Schön, W. Warta, S. W. Glunz, and M. C. Schubert, "Degradation of crystalline silicon due to boron–oxygen defects," *IEEE J. Photovolt.*, vol. 7, no. 1, pp. 383–398, Jan. 2017.

[21] J. A. Giesecke, M. C. Schubert, B. Michl, F. Schindler, and W. Warta, "Minority carrier lifetime imaging of silicon wafers calibrated by quasi-steady-state photoluminescence," *Sol. Energy Mater. Sol. Cells*, vol. 95, no. 3, pp. 1011–1018, 2011.

[22] M. Selinger *et al.*, "Spatially resolved analysis of light induced degradation of multicrystalline PERC solar cells," *Energy Procedia*, vol. 92, pp. 867–872, 2016.

[23] D. Macdonald, J. Tan, and T. Trupke, "Imaging interstitial iron concentrations in boron-doped crystalline silicon using photoluminescence," *J. Appl. Phys.*, vol. 103, no. 7, 2008, Art. no. 073710.

[24] J. D. Murphy, K. Bothe, V. V. Voronkov, and R. J. Falster, "On the mechanism of recombination at oxide precipitates in silicon," *Appl. Phys. Lett.*, vol. 102, no. 4, 2013, Art. no. 042105.

[25] J. Veirman *et al.*, "Novel way to assess the validity of czochralski growth simulations," *Phys. Status Solidi*, vol. 216, Sep. 2019, Art. no. 1900317.

[26] V. V. Voronkov, "The mechanism of swirl defects formation in silicon," *J. Cryst. Growth*, vol. 59, no. 3, pp. 625–643, 1982.

[27] J. D. Murphy, K. Bothe, R. Krain, V. V. Voronkov, and R. J. Falster, "Parameterisation of injection-dependent lifetime measurements in semiconductors in terms of Shockley-Read-Hall statistics: An application to oxide precipitates in silicon," *J. Appl. Phys.*, vol. 111, no. 11, 2012, Art. no. 113709.

[28] J. Schön *et al.*, "Identification of lifetime limiting defects by temperature- and injection-dependent photoluminescence imaging," *J. Appl. Phys.*, vol. 120, no. 10, 2016, Art. no. 105703.

[29] B. Hallam, C. Chan, M. Abbott, and S. Wenham, "Hydrogen passivation of defect-rich n-type Czochralski silicon and oxygen precipitates," *Sol. Energy Mater. Sol. Cells*, vol. 141, pp. 125–131, 2015.

[30] K. Bothe, R. Sinton, and J. Schmidt, "Fundamental boron-oxygen-related carrier lifetime limit in mono- and multicrystalline silicon," *Prog. Photovolt., Res. Appl.*, vol. 13, no. 4, pp. 287–296, 2005.

[31] B. Michl, J. Schön, W. Warta, and M. C. Schubert, "The impact of different diffusion temperature profiles on iron concentrations and carrier lifetimes in multicrystalline silicon wafers," *IEEE J. Photovolt.*, vol. 3, no. 2, pp. 635–640, Apr. 2013.

[32] R. J. Falster, M. Cornara, D. Gambaro, M. Olmo, and M. Pagani, "Effect of high temperature pre-anneal on oxygen precipitates nucleation kinetics in Si," *Solid State Phenomena*, vol. 57/58, pp. 123–128, 1997.

[33] P. J. Cousins and J. E. Cotter, "The influence of diffusion-induced dislocations on high efficiency silicon solar cells," *IEEE Trans. Electron Devices*, vol. 53, no. 3, pp. 457–464, Mar. 2006.